Manifestations of classical size effect and electronic viscosity in the magnetoresistance of narrow two-dimensional conductors: Theory and experiment

O. E. Raichev,[1] G. M. Gusev,[2] A. D. Levin,[2] and A. K. Bakarov[3,4]
[1]*Institute of Semiconductor Physics, NAS of Ukraine, Prospekt Nauki 41, 03028 Kyiv, Ukraine*
[2]*Instituto de Física da Universidade de São Paulo, 135960-170, São Paulo, SP, Brazil*
[3]*Institute of Semiconductor Physics, Novosibirsk 630090, Russia*
[4]*Novosibirsk State University, Novosibirsk 630090, Russia*

(Received 1 April 2020; revised manuscript received 20 May 2020; accepted 12 June 2020; published 22 June 2020)

We develop a classical kinetic theory of magnetotransport of 2D electrons in narrow channels with partly diffusive boundary scattering and apply it to the description of magnetoresistance measured in the temperature interval 4.2–30 K in long mesoscopic bars fabricated from high-purity GaAs quantum well structures. Both experiment and theory demonstrate a number of characteristic features in the longitudinal and Hall resistances caused by the size effect in two dimensions owing to the high ballisticity of the transport. In addition to the features described previously, we also reveal a change in the slope of the first derivative of magnetoresistance when the cyclotron orbit diameter equals to half of the channel width. These features are suppressed with increasing temperature as a result of the electronic viscosity due to electron-electron interaction. By comparing theory and experiment, we determine the characteristic time of relaxation of angular distribution of electrons caused by electron-electron scattering.

DOI: 10.1103/PhysRevB.101.235314

I. INTRODUCTION

In past years, numerous experimental and theoretical studies have revealed interesting effects in transport of two-dimensional (2D) electron systems under conditions when electron movement is affected by internal friction due to interaction between the particles and resembles the dynamics of viscous fluids [1–28]. Such effects become important even in the linear transport, provided that the electron system is spatially inhomogeneous and electron-electron interaction is sufficiently strong. The hydrodynamic transport regime can be detected, in particular, in narrow conducting channels (2D wires), when the mean free path of electrons with respect to momentum changing scattering by impurities and phonons, l_1, is larger than the channel width L, while the mean free path with respect to momentum conserving electron-electron scattering, l_e, is much smaller than both l_1 and L. Due to the dominance of electron-electron scattering over the other scattering processes, the standard Drude picture of transport becomes invalid. As it was found in the pioneering theoretical study by Gurzhi [1], in these conditions the ohmic resistivity should decrease with increasing temperature T in a certain interval of T and depend on the channel width. In 2D systems, a temperature-induced decrease of resistivity, attributed to the Gurzhi effect, was observed under conditions when electrons were heated by the current [2] and in a special (H-shaped) bar geometry [21]. More manifestations of electron viscosity in narrow 2D channels can be found in the presence of a transverse magnetic field B.

The features of narrow channel resistance associated with hydrodynamic transport are easier to observe in the systems with a large mean free path l_1, such as graphene and high-purity GaAs quantum wells with large electron densities $n_s \sim 10^{12}$ cm^{-2}, though in both cases one requires elevated electron temperatures $T \sim 100$ K to enable strong electron-electron scattering. At lower temperatures, the transport regime is intermediate between hydrodynamic and quasiballistic regimes. A purely hydrodynamic approach to transport, implying a solution of the linearized Navier-Stokes equation with boundary conditions for electron current or drift velocity [10], is insufficient in this case. Thus, a description of transport properties should be based on a more detailed approach assuming solution of the Boltzmann kinetic equation complemented with the boundary conditions for the electron distribution function. The kinetic equation approach is valid for an arbitrary hierarchy of the characteristic lengths l_e, l_1, and L, so the standard diffusive (Drude), ballistic (Knudsen), and hydrodynamic (Poiseuille) transport regimes follow as limiting cases of the general description. With a simplifying relaxation-time approximation for the electron-electron collision integral, the kinetic equation is reduced to a differential equation and allows for either analytical or numerical solution [2,3,14,17,19,24–26,28]. In the presence of a magnetic field, however, the problem still remains complicated, as the kinetic equation is a partial differential equation involving the derivatives over both spatial coordinates and electron momentum. This problem has been recently solved in the geometry of an infinitely long 2D channel, when the distribution function depends only on one spatial coordinate. A numerical solution has been obtained by using the method of characteristics together with the boundary conditions for fully diffusive scattering on the edges (boundaries) [14]. An approximate perturbative solution with similar boundary conditions has been found for the case of small magnetic fields [24,25]. A

numerical solution by the method of characteristics has also been obtained for a more realistic case of partly diffusive scattering at the edges [28]. However, the boundary conditions proposed in Ref. [28] are not justified from a microscopic consideration of electron scattering at the edge and do not guarantee the necessary requirement of zero flux of electrons through the edge.

In this paper, we further develop the theory of magnetotransport in narrow conducting channels by applying reliable boundary conditions for the solution of the kinetic equation. Then we carry out a detailed comparison of the results of theoretical calculations with experimental magnetotransport data, which has not been done in previous works. Such a comparison allows us to investigate both the classical size effect and the influence of viscosity on magnetotransport properties in a wide temperature range on an equal footing. This leads us to a deeper understanding of the roles of boundary scattering and electron-electron interaction in transport of bounded 2D fermion systems and provides an estimate for electron-electron scattering time characterizing momentum relaxation of electron distribution.

The paper is organized as follows. In Sec. II we describe the theoretical model and present some results of its application. Section III contains description of measurements, presentation of experimental and theoretical results, and their comparison and discussion. More discussion and concluding remarks are given in the last section. The Appendix provides the details of the solution of the kinetic equation by the method of characteristics.

II. THEORY

The classical kinetic equation for the distribution function $f_{\mathbf{p}}(\mathbf{r})$ in the electric field $\mathbf{E}(\mathbf{r}) = -\nabla\Phi(\mathbf{r})$ (Φ is the electrostatic potential) and homogeneous magnetic field $\mathbf{B}$ directed perpendicular to the 2D plane is

$$\mathbf{v}\cdot\nabla f_{\mathbf{p}}(\mathbf{r}) + \left(e\mathbf{E}(\mathbf{r}) + \frac{e}{c}[\mathbf{v}\times\mathbf{B}]\right)\cdot\frac{\partial}{\partial\mathbf{p}} f_{\mathbf{p}}(\mathbf{r}) = \mathcal{J}_{\mathbf{p}}(\mathbf{r}), \quad (1)$$

where $\mathbf{r} = (x, y)$ and $\mathbf{p}$ are the coordinate and momentum of electrons, e is the electron charge, and c is the light velocity. For electrons with isotropic and parabolic spectrum, the velocity is given by $\mathbf{v} = \mathbf{p}/m$, where m is the effective mass. The right-hand side of Eq. (1) contains the collision integrals specified below. Instead of two components of $\mathbf{p}$, it is convenient to use energy and angle variables according to $\mathbf{p} = mv_\varepsilon(\cos\varphi, \sin\varphi)$ so that $f_{\mathbf{p}}(\mathbf{r}) \equiv f_{\varepsilon\varphi}(\mathbf{r})$, where φ is the angle between the x axis and the direction of momentum.

Assume that there is a boundary $y = y_0$ and electrons occupy the region above the boundary, $y > y_0$. If boundary scattering of electrons is elastic and not influenced by the magnetic field, the most general boundary condition for the distribution function $f_{\varepsilon\varphi}(\mathbf{r})$ at the boundary $\mathbf{r} = (x, y_0)$ takes the form

$$f_{\varepsilon\varphi} = \mathrm{r}_{\varepsilon\varphi} f_{\varepsilon 2\pi-\varphi} + \int_0^\pi \frac{d\varphi'}{\pi}\sin\varphi' P_\varepsilon(\varphi,\varphi') f_{\varepsilon 2\pi-\varphi'},$$
$$\mathrm{r}_{\varepsilon\varphi} = 1 - \int_0^\pi \frac{d\varphi'}{\pi}\sin\varphi' P_\varepsilon(\varphi,\varphi'),\ \varphi\in[0,\pi]. \quad (2)$$

The left-hand side of this equation presents the distribution function of reflected electrons, for which $\varphi \in [0, \pi]$. The right-hand side is expressed through the distribution function of incident electrons, part of which is reflected specularly. The probability of specular scattering is characterized by the reflection coefficient $\mathrm{r}_{\varepsilon\varphi}$. The function $P_\varepsilon(\varphi, \varphi')$ is determined by the properties of boundary scattering. It is symmetric with respect to permutation of variables, $P_\varepsilon(\varphi, \varphi') = P_\varepsilon(\varphi', \varphi)$, and goes to zero at $\varphi = 0$ and $\varphi = \pi$ because the boundary does not affect the electrons moving parallel to it. Equation (2) can be obtained by a direct adoption of the boundary conditions derived for three-dimensional electrons [29–31] to the case of 2D electrons. This equation automatically guarantees zero particle flux through the boundary, $\int_0^{2\pi} d\varphi v_y f_{\varepsilon\varphi} = v_\varepsilon\int_0^\pi d\varphi\sin\varphi(f_{\varepsilon\varphi} - f_{\varepsilon 2\pi-\varphi}) = 0$. Under certain conditions, the symmetry of the distribution function makes the integral term in Eq. (2) equal to zero, and the boundary condition takes a simple form, $f_{\varepsilon\varphi} = \mathrm{r}_{\varepsilon\varphi} f_{\varepsilon 2\pi-\varphi}$, similar to that proposed by Fuchs [32]. Such a case is realized, for example, in the geometry of a long and narrow channel at zero magnetic field [2,29]. The case of fully specular boundary scattering corresponds to $P_\varepsilon(\varphi, \varphi') = 0$ so that $\mathrm{r}_{\varepsilon\varphi} = 1$. A fully diffusive boundary scattering means $\mathrm{r}_{\varepsilon\varphi} = 0$ (except for the angles $\varphi = 0$ and $\varphi = \pi$) and Eq. (2) takes the form [33]

$$f_{\varepsilon\varphi} = \frac{1}{2}\int_0^\pi d\varphi'\sin\varphi' f_{\varepsilon 2\pi-\varphi'},\ 0<\varphi<\pi. \quad (3)$$

The function $P_\varepsilon(\varphi, \varphi')$ can be representable as a product of two functions of φ and φ', so the kernel in Eq. (2) is degenerate. Physically, this case corresponds to uncorrelated boundary scattering, when the scattering probability does not depend on the difference between the momenta of incoming and reflected particles. The boundary condition then can be written in terms of the reflection coefficient $\mathrm{r}_{\varepsilon\varphi}$ only:

$$f_{\varepsilon\varphi} = \mathrm{r}_{\varepsilon\varphi} f_{\varepsilon 2\pi-\varphi} + (1-\mathrm{r}_{\varepsilon\varphi})M,\ \varphi\in[0,\pi], \quad (4)$$

where M is a constant,

$$M = \frac{1}{\mathcal{N}}\int_0^\pi d\varphi\sin\varphi(1-\mathrm{r}_{\varepsilon\varphi}) f_{\varepsilon 2\pi-\varphi},$$
$$\mathcal{N} = \int_0^\pi d\varphi\sin\varphi(1-\mathrm{r}_{\varepsilon\varphi}). \quad (5)$$

Naturally, the limiting transition $\mathrm{r}_{\varepsilon\varphi}\to 0$ transforms Eq. (4) into Eq. (3). The boundary condition Eq. (4) will be applied below in the calculations.

In this paper, we consider infinitely long 2D channels of width L ($0 < y < L$, $-\infty < x < \infty$), Fig. 1. Such a model can be applied to samples whose length is much larger than their width. In these conditions, the electron system is homogeneous along the x direction so that the distribution function depends only on the y coordinate, and the electrostatic potential is representable in the form $\Phi(\mathbf{r}) = -Ex + \Phi(y)$, where $E \equiv E_x$ is a homogeneous electric field. Considering the linear response problem, it is convenient to write the distribution function as

$$f_{\varepsilon\varphi}(\mathbf{r}) = f_\varepsilon - \frac{\partial f_\varepsilon}{\partial\varepsilon}[g_{\varepsilon\varphi}(y) - e\Phi(y)], \quad (6)$$

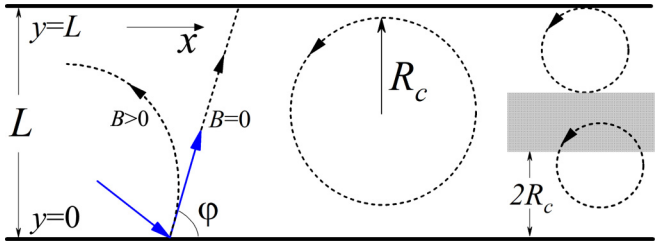

FIG. 1. Illustration of electron motion in the 2D channel. The diffusive boundary scattering of electrons increases the resistance. A deflection of ballistic electron paths (dashed lines) by magnetic field decreases the probability of boundary scattering. At $R_c < L/2$, some electrons are moving in cyclotron orbits and do not hit the boundaries. At $R_c < L/4$, all the electrons whose ballistic paths pass through the region $2R_c < y < L - 2R_c$ (shaded) do not hit the boundaries.

where f_ε is the equilibrium Fermi distribution and $g_{\varepsilon\varphi}$ describes a small nonequilibrium part of the distribution function. Substituting Eq. (6) into Eq. (1), one gets the linearized kinetic equation for $g_{\varepsilon\varphi}$:

$$\left[\sin\varphi\frac{\partial}{\partial y}g_{\varepsilon\varphi}(y) + R_{c\varepsilon}^{-1}\frac{\partial}{\partial\varphi}g_{\varepsilon\varphi}(y) - eE\cos\varphi\right] \times\left(\frac{\partial f_\varepsilon}{\partial\varepsilon}\right) + \frac{\mathcal{J}_{\varepsilon\varphi}(y)}{v_\varepsilon} = 0, \tag{7}$$

where $R_{c\varepsilon}$ is the classical cyclotron radius for an electron with energy ε and

$$\mathcal{J}_{\varepsilon\varphi}(y) = -\frac{\partial f_\varepsilon}{\partial\varepsilon}\left[J^{im}_{\varepsilon\varphi}(y) + J^{ph}_{\varepsilon\varphi}(y) + J^{ee}_{\varepsilon\varphi}(y)\right]$$

is the linearized collision integral describing interaction of electrons with impurities (im) and phonons (ph) as well as electron-electron (ee) interaction. In the transformations, we have used the equality $E_y(\mathbf{r}) = -\partial\Phi(y)/\partial y$ and divided the kinetic equation by the velocity v_ε. It is easy to observe that $g_{\varepsilon\varphi}$ is governed by the same boundary condition, Eq. (4), since any angular-independent part of $f_{\varepsilon\varphi}(\mathbf{r})$ satisfies Eq. (4) automatically.

Further, we consider the case of degenerate electron gas, which means that the factor $-(\partial f_\varepsilon/\partial\varepsilon)$ in Eq. (7) represents a narrow peak around the Fermi energy ε_F. Assuming that scattering times in the bulk and the boundary reflection coefficients do not change appreciably within the temperature-size energy interval around ε_F, one can replace $-(\partial f_\varepsilon/\partial\varepsilon)$ by the delta function $\delta(\varepsilon - \varepsilon_F)$ and integrate Eq. (7) over energy, which is equivalent to substitution of ε by ε_F, so the energy index below will be omitted. The relative corrections to the resistance caused by the thermal broadening of the Fermi distribution are of the order $(T/\varepsilon_F)^2$ and, therefore, are not significant. The electron-electron part of the linearized collision integral is written in the relaxation-time approximation [2,3,14,17,19,28]:

$$J^{ee}_\varphi(y) = -\frac{g_\varphi(y) - g_0(y) - g_1(y)\cos\varphi - \tilde{g}_1(y)\sin\varphi}{\tau_e}, \tag{8}$$

where τ_e is the effective electron-electron scattering time, and

$$g_0 = \overline{g_\varphi},\ g_1 = 2\overline{g_\varphi\cos\varphi},\ \tilde{g}_1 = 2\overline{g_\varphi\sin\varphi}. \tag{9}$$

Here, $\overline{F}_\varphi \equiv (2\pi)^{-1}\int_0^{2\pi} d\varphi F_\varphi$ denotes angular averaging. The quantities $g_1(y)$ and $\tilde{g}_1(y)$ are proportional to local electric currents along x and y directions. Note, however, that in the geometry under consideration the current flows only in the x direction, because only in this case the requirement of zero flux through the boundary is compatible with the continuity equation, so $\tilde{g}_1(y) = 0$. A similar relaxation-time approximation is applied for the momentum changing (electron-impurity and electron-phonon) parts of the collision integral:

$$J^{im}_\varphi(y) + J^{ph}_\varphi(y) = -\frac{g_\varphi(y) - g_0(y)}{\tau_{tr}}, \tag{10}$$

where τ_{tr} is the transport time. The times τ_{tr} and τ_e characterize relaxation of nonequilibrium distribution over the angle of electron momentum. As follows from Eqs. (8) and (10), τ_{tr} describes relaxation of all angular harmonics of the distribution function except the zero one (g_0), while τ_e describes relaxation of all angular harmonics except the zero and the first ones. Though the introduction of the unified times for all harmonics is a crude approximation, it enormously simplifies solution of the kinetic equation.

Combining Eqs. (7), (8), and (10), we introduce characteristic mean free path lengths $l_1 = v\tau_{tr}$, $l_e = v\tau_e$, and $l = (1/l_1 + 1/l_e)^{-1}$ and write the linearized kinetic equation in the form

$$\left[\sin\varphi\frac{\partial}{\partial y} + R_c^{-1}\frac{\partial}{\partial\varphi} + \frac{1}{l}\right]g_\varphi(y) = \frac{g_0(y)}{l} + \frac{g_1(y)\cos\varphi}{l_e} + eE\cos\varphi \equiv \mathcal{F}_\varphi(y). \tag{11}$$

This partial differential equation describes the distribution function in the channel $0 < y < L$ with the boundary conditions [see Eq. (4)] written below for $\varphi \in [0, \pi]$:

$$g_\varphi(0) = \mathrm{r}^0_\varphi g_{2\pi-\varphi}(0) + \left(1 - \mathrm{r}^0_\varphi\right)M_0, \tag{12}$$

$$g_{2\pi-\varphi}(L) = \mathrm{r}^L_\varphi g_\varphi(L) + \left(1 - \mathrm{r}^L_\varphi\right)M_L. \tag{13}$$

The two boundaries, in general, can be different, so they are characterized by different reflection coefficients, r^0_φ for $y = 0$ and r^L_φ for $y = L$. The constants in Eqs. (12) and (13) are

$$M_0 = \frac{1}{\mathcal{N}_0}\int_0^\pi d\varphi\sin\varphi\left(1 - \mathrm{r}^0_\varphi\right)g_{2\pi-\varphi}(0),$$

$$M_L = \frac{1}{\mathcal{N}_L}\int_0^\pi d\varphi\sin\varphi\left(1 - \mathrm{r}^L_\varphi\right)g_\varphi(L),$$

$$\mathcal{N}_{0,L} = \int_0^\pi d\varphi\sin\varphi\left(1 - \mathrm{r}^{0,L}_\varphi\right). \tag{14}$$

The cyclotron radius at the Fermi level is determined by the magnetic field and electron density n_s, since $R_c = \ell^2 k_F$, where $\ell = \sqrt{\hbar c/|e|B}$ is the magnetic length, $k_F = \sqrt{4\pi n_s/\mathrm{g}}$ is the Fermi wave number, and g is the band degeneracy factor (g = 2 for GaAs quantum wells). Thus, Eqs. (11)–(14) do not contain parameters related to band dispersion and can be applied to any kind of fermion, including electrons in graphene (where g = 4 due to both spin and valley degeneracy).

The problem described by Eqs. (11)–(14) is solved by the method of characteristics as described in the Appendix. Such a solution allows us to reduce the problem to a pair of coupled

Fredholm integral equations for the functions of one variable, $g_0(y)$ and $g_1(y)$:

$$g_0(y) = eE\mathcal{L}_0(y) + \frac{1}{l}\int_0^L dy'\mathcal{K}_{00}(y,y')g_0(y') + \frac{1}{l_e}\int_0^L dy'\mathcal{K}_{01}(y,y')g_1(y'), \quad (15)$$

$$g_1(y) = eE\mathcal{L}_1(y) + \frac{1}{l}\int_0^L dy'\mathcal{K}_{10}(y,y')g_0(y') + \frac{1}{l_e}\int_0^L dy'\mathcal{K}_{11}(y,y')g_1(y'), \quad (16)$$

where the four kernels $\mathcal{K}_{nn'}$ and the functions $\mathcal{L}_n$ are given in the Appendix. If electron-electron interaction is neglected, $l_e \to \infty$, the terms with $\mathcal{K}_{01}$ and $\mathcal{K}_{11}$ disappear, and the first equation decouples from the second one. In this limit, the theory describes a classical size effect without viscosity corrections. In the limit $B = 0$, the terms with $\mathcal{K}_{01}$, $\mathcal{K}_{10}$, and $\mathcal{L}_0$ disappear so that $g_0(y) = 0$ and only one integral equation remains:

$$g_1(y) = eE\mathcal{L}_1(y) + \frac{1}{l_e}\int_0^L dy'\mathcal{K}_{11}(y,y')g_1(y'). \quad (17)$$

This equation is identical to the one derived in Ref. [2], see the Appendix for details. It describes effects of viscosity on the transport at zero magnetic field.

A numerical solution of Eqs. (15) and (16) determines $g_0(y)$ and $g_1(y)$ as a response to the electric field E. Such a solution is obtained by a direct application of linear algebra (200-point discretization of the variable y/L is sufficient in most cases). A solution by the method of iterations gives the same output. To control the accuracy of the procedure, the quantity $\tilde{g}_1(y) = 2\overline{g_\varphi(y)\sin\varphi}$, which is proportional to the current along the y axis and must be zero, is calculated simultaneously. At the edges $y = 0$ and $y = L$, $\tilde{g}_1(y)$ is exactly zero, as dictated by the boundary conditions, while in the bulk it is finite because of computational errors but always stays several orders of magnitude smaller than $g_1(y)$.

The quantity $g_1(y)$, as already noted, describes spatial distribution of electric current density $j(y)$. On the other hand, the quantity $g_0(y)$ describes spatial distribution of the electrochemical potential, i.e., the local voltage $V(y)$. To show this, we note that the latter is defined as $V(y) = \Phi(y) + \delta\mu(y)/e$, where $\delta\mu$ is the nonequilibrium part of the local chemical potential. By definition, $\delta\mu(y) = \delta n_s(y)/\rho_{2D}$, where δn_s is the nonequilibrium part of local electron density and $\rho_{2D} = m/\pi\hbar^2$ is the density of states for 2D electrons. Thus, $\delta\mu(y) = \int d\varepsilon(\overline{f_{\varepsilon\varphi}(y)} - f_\varepsilon) \simeq g_0(y) - e\Phi(y)$, according to Eq. (6). In summary,

$$j(y) = emvg_1(y)/2\pi\hbar^2, \quad V(y) = g_0(y)/e. \quad (18)$$

These two variables is all we need to find both the longitudinal and the Hall resistance. Though the presence of electric field E along the channel induces y-dependent electrostatic potential $\Phi(y)$ and the nonequilibrium part of electron density $\delta n_s(y)$, which can be determined by involving the Poisson's equation, we do not need them for description of the resistance within the approximations used: the classical transport regime, the linear response regime, and the case of degenerate electron gas.

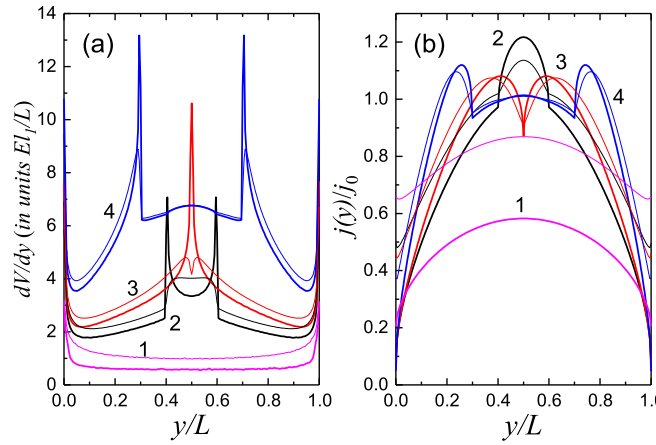

FIG. 2. Distribution of the Hall field $dV(y)/dy$ (a) and current density (b) at $l_1/L = 3$ for several values of magnetic field, $R_c/L = 0.6$ (1), 0.3 (2), 0.25 (3), 0.15 (4), in the absence of electron-electron scattering. The current density is expressed in units of the bulk current density j_0. Sharp features of the distributions associated with ballistic transport appear at $y = 2R_c$ and $y = L - 2R_c$. The bold lines show the case of fully diffusive boundary scattering, $\mathrm{r}_\varphi^0 = \mathrm{r}_\varphi^L = 0$, while the thin lines correspond to weakly diffusive boundaries, $\mathrm{r}_\varphi^0 = \mathrm{r}_\varphi^L = \exp(-\alpha\sin^2\varphi)$ with $\alpha = 1$.

In the homogeneous case (far away from the boundaries of a wide sample), the solutions of Eqs. (15) and (16) are $g_1(y) = eEl_1$ and $g_0(y) = C + eEl_1y/R_c$ (here C is a constant), corresponding to the bulk Drude conductivity and constant Hall electric field (see the final part of the Appendix for details).

The examples of calculation of the current and Hall voltage distributions across the 2D channels with a high ballisticity, $l_1/L = 3$, are shown in Figs. 2 and 3. Instead of $V(y)$, its derivative (Hall field) is plotted in order to emphasize sharp features of the distributions appearing at $2R_c < L$ [28]. These features are associated with ballistic motion of electrons in cyclotron orbits. They become weaker with increasing specularity of the boundary scattering and tend to disappear when electron-electron interaction becomes strong so that the transport enters the hydrodynamic regime [28]. As shown in Fig. 3, the distributions approach the ones calculated in the hydrodynamic approximation [10]:

$$j(y) = j_0\{1 - \lambda\cosh[\kappa(y - L/2)]\},$$
$$\frac{dV(y)}{dy} = \frac{El_1}{R_c}\{1 - (1 + 2l/l_1)\lambda\cosh[\kappa(y - L/2)]\},$$
$$\kappa = 2\sqrt{\frac{1 + (2l/R_c)^2}{ll_1}}, \quad \lambda = \frac{1}{\cosh\frac{\kappa L}{2} + \kappa l_s\sinh\frac{\kappa L}{2}}, \quad (19)$$

where j_0 is the bulk current density and l_s is the slip length entering the boundary conditions $j(y) = \pm l_s\partial j(y)/\partial y$ at $y = 0$ and $y = L$. The distributions become closer to the hydrodynamic ones as the magnetic field increases. However, near the boundaries the Hall field is still considerably different from that following from the hydrodynamic theory.

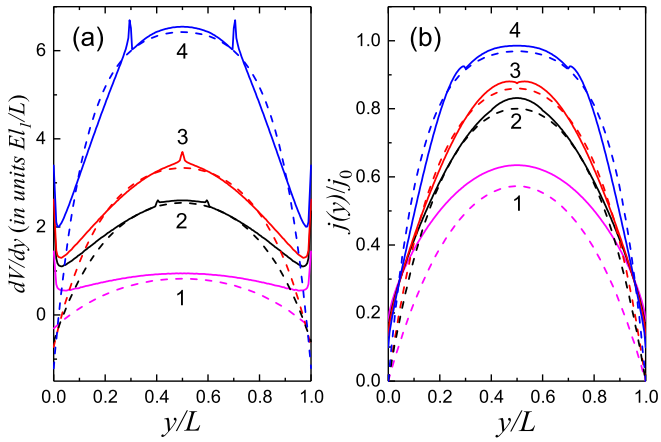

FIG. 3. Distribution of the Hall field $dV(y)/dy$ (a) and current density (b) at $l_1/L = 3$ for several values of magnetic field, $R_c/L =$ 0.6 (1), 0.3 (2), 0.25 (3), 0.15 (4), when the electron-electron scattering is strong, $l_1/l_e = 10$. The solid lines correspond to calculations for fully diffusive boundary scattering. The dashed lines show the result of application of hydrodynamic approximation under the "no-slip" boundary condition, $j(0) = j(L) = 0$ ($l_s = 0$), see Eq. (19). The sharp features of the distributions are suppressed by the viscosity effect.

When the current and the voltage distributions are found, one can determine the total current $I = \int_0^L dy j(y)$ and the Hall voltage $V_H = V(L) - V(0)$ as linear functions of the electric field E and to find the longitudinal resistance R_{xx} and the Hall resistance R_{xy}. A comparison of the results of such calculations to experimental data is described in the next section. In Figs. 4–7, we present some results demonstrating the general features of the behavior of R_{xx} and $\Delta R_{xy} = R_{xy} - R_{xy}^{(0)}$, expressed in units of classical bulk resistances R_0 and $R_{xy}^{(0)} = B/|e|cn_s$. The magnetic field B is expressed through the ratio $L/R_c \propto B$. We consider the dependence of magnetoresistance on the boundary reflection properties, ballisticity ratio l_1/L,

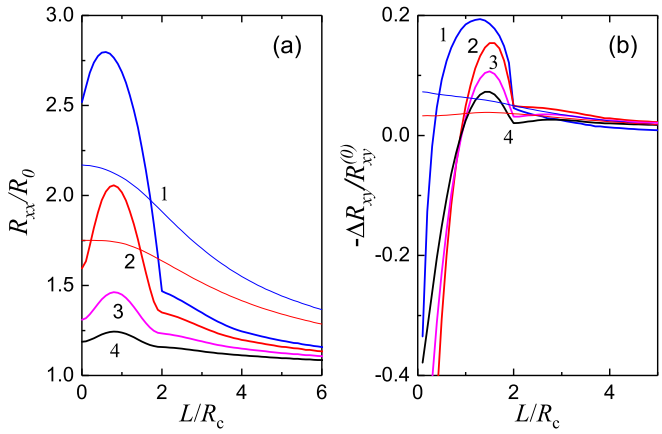

FIG. 4. Longitudinal (a) and Hall (b) resistance at $l_1/L =$ 3 for angular-dependent boundary reflection coefficient $r_\varphi = \exp(-\alpha \sin^2 \varphi)$ with $\alpha = \infty$ (fully diffusive, 1), $\alpha = 3$ (2), $\alpha = 1$ (3), and $\alpha = 0.5$ (4). Bold lines: $l_1/l_e = 0$ (no electron-electron scattering), thin lines (plotted for 1 and 2 only): $l_1/l_e = 10$.

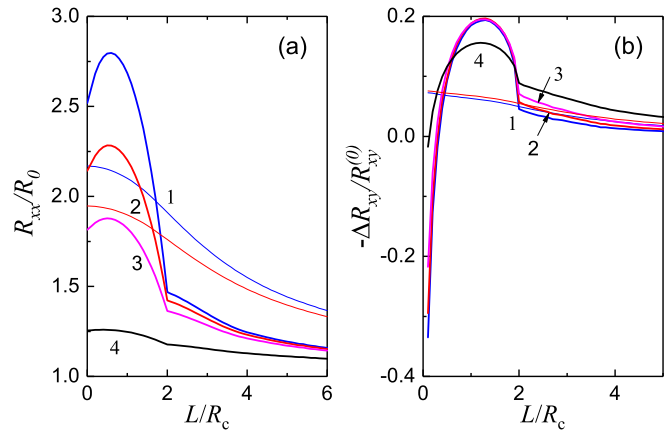

FIG. 5. The same as in Fig. 4 for constant (angular-independent) boundary reflection coefficient $r_\varphi = r$ with r = 0 (fully diffusive, 1), r = 0.2 (2), r = 0.4 (3), and r = 0.8 (4).

and relative strength of electron-electron scattering l_1/l_e. The boundaries are assumed to be equivalent, $r_\varphi^0 = r_\varphi^L \equiv r_\varphi$.

The basic features of the plots are the manifestations of the classical size effect due to quasiballistic propagation of 2D electrons in the channel in the presence of a magnetic field. They include peaks of both R_{xx} and $-\Delta R_{xy}/R_{xy}^{(0)}$, whose maxima are placed at finite magnetic fields, and a sharp decrease of the magnetoresistance slope when the cyclotron diameter $2R_c$ becomes smaller than L. The behavior of R_{xx} was initially described for three-dimensional thin films [34] and also observed in submicron-wide 2D channels [35], while the behavior of R_{xy} was described recently within the model of fully diffusive boundary scattering [14]. At small B, the resistance increases because the magnetic field deflects the electrons which move at sliding angles (φ close to 0 or π) and provide a significant contribution to the current. A further increase of B, on the contrary, decreases the probability of electron collisions with the boundaries, thereby leading to a rapid decrease of the resistance. When $2R_c$ becomes smaller than L, there appear electrons which do not collide with boundaries during their cyclotron motion, while the electrons scattered by one boundary cannot reach the other one unless they are scattered in the bulk. As a result, the decrease of the resistance with B slows down considerably.

Figures 4 and 5 correspond to two different models of boundary reflection. They show a decrease of the resistance peaks as the specularity increases. The model of angular-dependent boundary reflection, $r_\varphi = \exp(-\alpha \sin^2 \varphi)$ [29], gives deeper local minima of both R_{xx} and $-\Delta R_{xy}/R_{xy}^{(0)}$ at $B = 0$ because it provides larger probabilities of specular scattering at sliding angles. In the model of angular-independent reflection, the Hall resistance at $2R_c > L$ is almost insensitive to r in the region $r < 0.5$, if electron-electron scattering is absent. Figure 6 demonstrates a rapid decrease of the resistance peaks when the ballisticity ratio l_1/L goes down. The increasing specularity and decreasing ballisticity suppress the peaks but do not lead to broadening of these peaks and do not remove the local minimum at $B = 0$. On the other hand, the increase in electron-electron scattering probability, which takes place with increasing temperature, not only decreases the height of

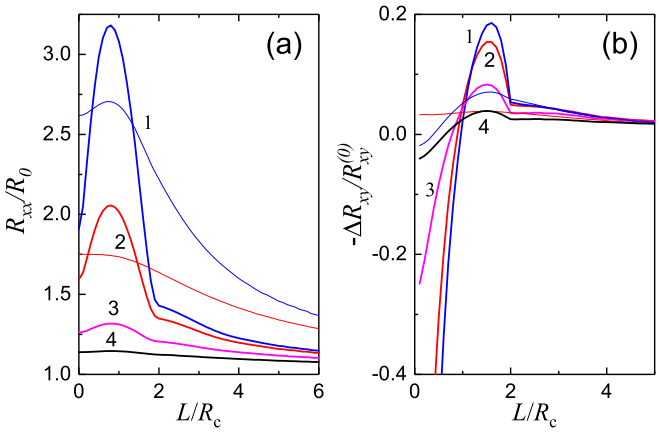

FIG. 6. Longitudinal (a) and Hall (b) resistance for the case of angular-dependent boundary reflection with $\alpha = 3$: $l_1/L = 6$ (1), 3 (2), 1 (3), and 0.5 (4). Bold lines: $l_1/l_e = 0$ (no electron-electron scattering), thin lines (plotted for 1 and 2 only): $l_1/l_e = 10$.

the peaks, but also considerably increases the peak width and leads to a weakening and eventual disappearance of the local minimum at $B = 0$. Notice also that the peak of $-\Delta R_{xy}/R_{xy}^{(0)}$ is suppressed more rapidly than the peak of R_{xx}. This influence is shown in detail in Fig. 7, which also demonstrates a nonmonotonic dependence of zero-B longitudinal resistance on l_1/l_e. As the electron-electron scattering increases, the electron system shifts towards the hydrodynamic regime, when the Gurzhi effect [1] is possible at $B = 0$ and the dependence of R_{xx} on B correlates with the corresponding dependence of the kinematic viscosity [10]. Thus, one can say that the modifications of the resistance shown in Fig. 7 are manifestations of viscosity effects; see also similar results [14] obtained within the model of fully diffusive boundary scattering. Our experimental data are in a good agreement with the behavior discussed above, as presented in more detail in the following section.

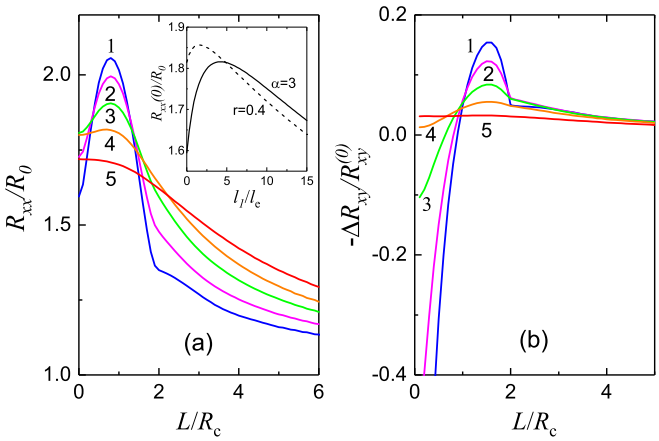

FIG. 7. Longitudinal (a) and Hall (b) resistance at $l_1/L = 3$, for angular-dependent boundary reflection with $\alpha = 3$: $l_1/l_e = 0$ (1), 1 (2), 3 (3), 6 (4), and 12 (5). The inset shows the resistance at $B = 0$ vs l_1/l_e for angular-dependent boundary reflection with $\alpha = 3$ (solid) and for angular-independent boundary reflection with r = 0.4 (dash).

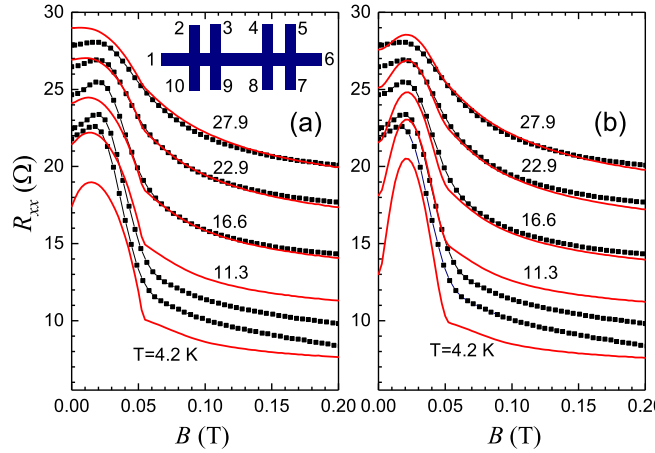

FIG. 8. Experimental (points) and calculated (lines) longitudinal resistance in the 5-μm-wide mesoscopic Hall bar (see the parameters in the text), measured between contacts 4 and 5 at different temperatures $T = 4.2$, 11.3, 16.6, 22.9, and 27.9 K. Results of calculations in the parts (a) and (b) correspond to two different models of boundary reflection, $r_\varphi = r = 0.35$ and $r_\varphi = \exp(-\alpha \sin^2 \varphi)$ with $\alpha = 3$.

III. COMPARISON OF THEORY WITH EXPERIMENT

We have investigated several samples in the form of long mesoscopic Hall bars of several micron widths with eight symmetrically placed voltage probes (see the inset in Fig. 8). The samples were fabricated from high-quality GaAs quantum wells with a width of 14 nm. The measurements were carried out in a VTI cryostat, using a conventional lock-in technique to measure the resistances with a sufficiently low ac current of 0.1–1.0 μA passed through contacts 1 and 6. Figure 8 shows a series of plots of longitudinal resistance versus magnetic field B in the region of small B, where classical magnetotransport is expected. The resistance is measured between contacts 4 and 5 (the distance between the centers of the corresponding side arms of the Hall bar is 9 μm, the width of the side arms is 3 μm at the entry to the channel) in the sample with the channel width $L = 5$ μm, electron density $n_s = 6.6 \times 10^{11}$ cm^{-2}, and mobility 2.1×10^6 cm^2/V s at $T = 4.2$ K. The density remains constant in the range of temperatures studied, and the corresponding Fermi energy, wave number, and velocity are 23.6 meV, 0.20 nm^{-1}, and 3.52×10^7 cm/s. The temperature dependence of resistance at $B = 0$ in macroscopic 2D samples (before shaping the mesoscopic Hall bars) was linear, $R \propto 1 + \beta T$, with $\beta \simeq 0.09$ K^{-1} above 4.2 K, due to the contribution of electron-phonon scattering into the transport. For these parameters, a high ballisticity is achieved, when the mean free path l_1 is larger than L even at $T \simeq 30$ K. Figure 9 shows the temperature dependence of l_1 for this sample and also for another sample described below.

All the experimental plots show characteristic peaks in the region of small B. An abrupt decrease of the peak slope at low temperatures occurs near $B \simeq 0.05$ T, which corresponds to $2R_c = L$ ($B = 0.053$ T). With increasing T, the relative height of the peak becomes smaller and the peak width increases. The maximum of the peak is placed at $B \simeq 0.02$ T. The local minimum at $B = 0$ tends to disappear at high temperatures. The observed weakening of the local minimum at $B = 0$, the

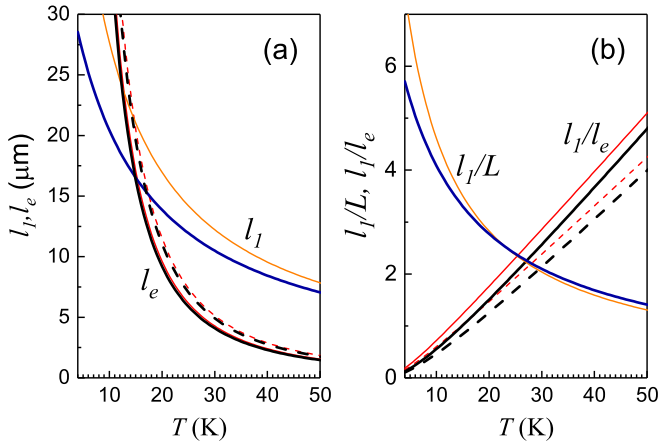

FIG. 9. Dependence of characteristic lengths l_1 and l_e (a) and of the ratios l_1/L and l_1/l_e (b) on temperature for the samples with $L = 5$ μm (bold lines) and $L = 6$ μm (thin lines). The length l_1 is extracted from the experimental dependence of bulk zero-B resistance on temperature, while the length l_e is evaluated according to Eq. (20) (solid and dashed lines correspond to $A = 5$ and $A = 6$, respectively).

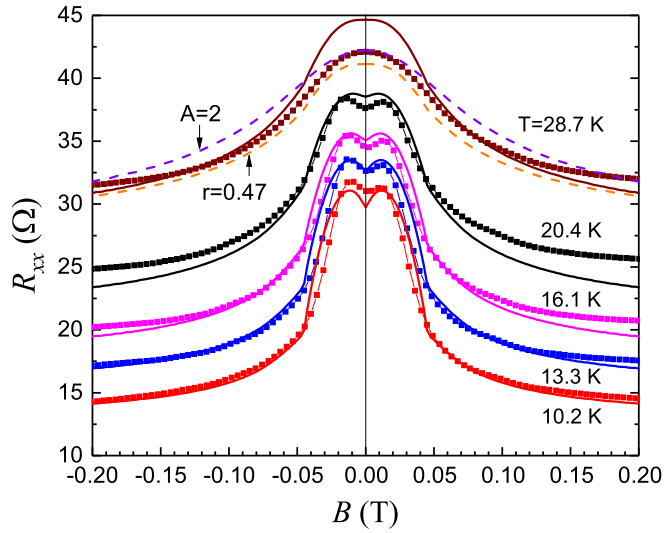

FIG. 10. Experimental (points) and calculated (lines) longitudinal resistance in the 6-μm-wide mesoscopic Hall bar (see the geometry in the inset to Fig. 8 and the parameters in the text), measured between contacts 3 and 4 at different temperatures indicated in the plot. The calculations correspond to the model of constant reflection coefficient, with r = 0.35 and $A = 6$ [the same as in Fig. 8(a)]. The dashed lines for $T = 28.7$ K are calculated with r = 0.47 and $A = 6$ and with r = 0.35 and $A = 2$.

decrease of the relative height of the peak, and the increase of the peak width with increasing T cannot be explained solely by a decrease of the transport mean free path length l_1 with increasing T. The contribution of electron-electron scattering turns out to be crucially important for description of the experiment.

Figure 8 also shows the results of calculations based on the parameters (L, n_s, mobility, aspect ratio, and coefficient β) of the sample described above. The boundaries are assumed to be equivalent, $r_\varphi^0 = r_\varphi^L \equiv r_\varphi$. The plots in Figs. 8(a) and 8(b) differ only by the model of boundary reflection. We have applied the models of a constant reflection coefficient $r_\varphi = r$ (a) and the angular-dependent one, in the form $r_\varphi = \exp(-\alpha \sin^2 \varphi)$ (b). The values of r and α have been considered as fitting parameters. The temperature dependence of the effective time of electron-electron scattering has been described by the formula

$$\tau_e = A\frac{\hbar\varepsilon_F}{T^2}. \tag{20}$$

We emphasize that τ_e, according to its introduction in Eq. (8), is the time of relaxation of electron distribution over the angles of electron momentum, and it is different from the quantum lifetime of electrons with respect to electron-electron scattering, though follows the same T^{-2} dependence. The numerical constant A is treated as another fitting parameter. The two fitting parameters, r and A (or α and A), have been varied to describe the heights and the shapes of the magnetoresistance peaks for the entire family of magnetoresistance curves plotted at different temperatures. The aspect ratio L_x/L, which is a constant scaling factor for all R_{xx} plots, was also adjusted by varying the effective distance L_x between the side arms of the Hall bar within the interval of the width of these arms, with the best fit for $L_x = 7.5$ μm. Since the magnetoresistance peak width is sensitive to τ_e and almost insensitive to r or α, such fits allow one to estimate the value of A with a good accuracy. The best fits are achieved for reasonable values r = 0.35 and $\alpha = 3$, with $A = 6$ for constant reflectivity and $A = 5$ for angular-dependent reflectivity. Decreasing A (i.e., increasing the contribution of electron-electron scattering) below these values leads to broader peaks and, consequently, to a worse agreement with the experiment at high T. An example of variation of r and A is shown in Fig. 10 (for the other sample) by the dashed lines.

In the region of low temperatures, $T < 12$ K, the T dependence of R_{xx} in the mesoscopic bars turns out to be slower than that for macroscopic samples. We attribute this effect to the mesoscopic nature of the contacts. Indeed, although in theory one can formally define the electrochemical potential (i.e., the local voltage) in each point of the 2D channel, it is not clear whether the voltage measured at the contact connected to the arm of the mesoscopic Hall bar corresponds to the voltage at the edge of the channel, especially when temperature is low. As a consequence, there are vertical shifts between calculated and experimental plots, since the calculations are based on the linear T dependence of R_{xx} obtained for macroscopic samples. Such shifts can be eliminated by proper scaling factors. As concerns the shape of magnetoresistance curves, the agreement between theory and experiment is reasonably good at all temperatures. The model of angular-dependent boundary reflection, which is apparently more realistic, gives a better agreement. However, this model strongly overestimates the depth of the observed local minima at $B = 0$, for which a better agreement is given by the model of constant reflection coefficient. The deep local minima similar to those in Fig. 8(b) have been found in earlier experiments on 2D channels with lower mobility and submicron widths [35].

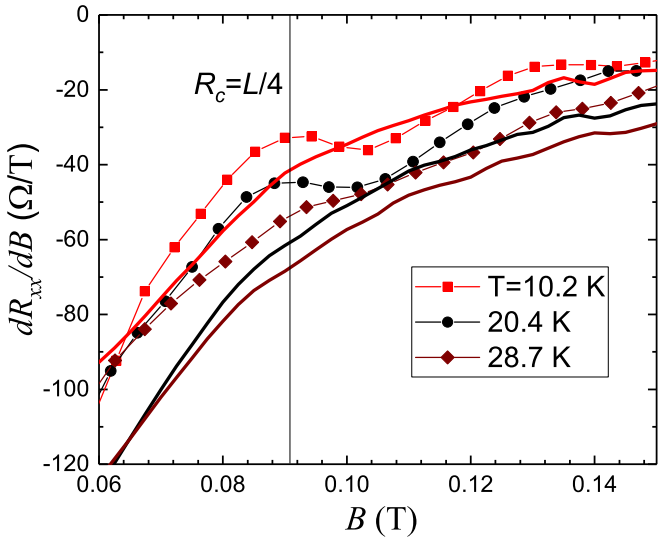

FIG. 11. First derivatives of the experimental (points) and calculated (lines) magnetoresistance in the 6 μm-wide mesoscopic Hall bar indicate a modification of transport behavior near the point $R_c = L/4$ (vertical line).

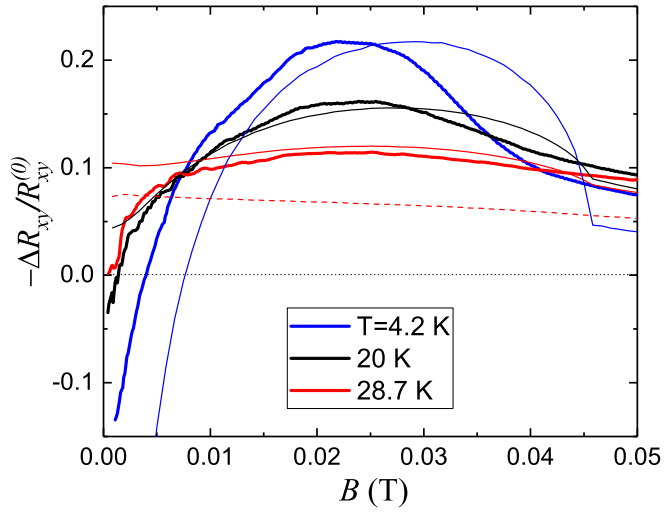

FIG. 12. Experimental (bold lines) and calculated (thin lines) normalized Hall resistance in the 6 μm-wide mesoscopic Hall bar (see the geometry in the inset to Fig. 8 and the parameters in the text) at different temperatures. The calculations correspond to the model of constant reflection coefficient, with r = 0.35 and $A = 6$, the dashed line shows the result for $T = 28.7$ K with $A = 2$.

In addition to the sample described above, we also studied a slightly wider mesoscopic bar, $L = 6$ μm, with density $n_s = 6.8 \times 10^{11}$ cm^{-2}, made from a structure with a higher mobility, 3.2×10^6 cm^2/V s at $T = 4.2$ K. For this sample, we have measured the resistance R_{xx} between contacts 3 and 4 (see the inset in Fig. 8) separated by 20 μm, and also the Hall resistance in the region of small B. Figure 10 presents the results of measurements together with theoretical plots for the model of angular-independent boundary scattering, calculated for the same parameters as those used in Fig. 8(a), r = 0.35 and $A = 6$. Again, we have a reasonable agreement between theory and experiment. For the high-temperature plot, the agreement can be improved by increasing r, which changes the relative height of the magnetoresistance peak without changing its shape, while a decrease of A makes the peak broader than the experimental one, see the dashed lines in Fig. 10.

Apart from the discussed manifestations of size effect, both the experimental and theoretical magnetoresistances at low temperatures demonstrate a weak modification of their slopes at $B = 0.091$ T, which corresponds to the condition $R_c = L/4$. As shown in Figs. 2 and 3, at this particular point both the current and the Hall field distributions exhibit sharp cusps at the center of the conducting channel. The cusps of the distributions recently became a subject of discussion [28], but their connection to magnetoresistance has not been examined either theoretically or experimentally. Meanwhile, a modification of magnetoresistance is expectable, because at $R_c < L/4$ there opens a region $2R_c < y < L - 2R_c$ containing the electrons whose ballistic trajectories do not reach any of the boundaries, see Fig. 1. To study the behavior of magnetoresistance in the vicinity of $R_c = L/4$, we have plotted the first derivatives of R_{xx}, shown in Fig. 11. The theoretical plot at low T shows a sharp change of the slope at $R_c = L/4$, which is equivalent to a sharp change of the second derivative of R_{xx}. The experimental plot demonstrates an even stronger feature: a change in the slope of dR_{xx}/dB includes an interval of nonmonotonic dependence near $R_c = L/4$. These features are apparently of the ballistic origin, and they are washed out by temperature when the transport approaches to the hydrodynamic regime, as shown by both theory and experiment. Similar modifications of the resistance are also present in the case when the resistance is measured between contacts 2 and 5 separated by 40 μm, but they are not seen in the measurements shown in Fig. 8, where the distance between the voltage contacts is close to L.

Finally, we describe the results of the Hall resistance measurements shown in Fig. 12. The theory predicts (see Ref. [14] and the results shown in Figs. 4–7) that ΔR_{xy} in the ballistic transport regime changes its sign in the region of low B. This property has been recently confirmed experimentally [22], and it is also seen in Fig. 12. The comparison of the present theory with experiment shows that the general behavior of the Hall resistance and the heights of the peaks of $-\Delta R_{xy}/R_{xy}^{(0)}$ are in agreement with theory. However, the experimental peaks are positioned at smaller magnetic field than the theoretical ones. We could not obtain a good fit to the shape of ΔR_{xy} by varying the adjustable parameters within the reasonable range. In any case, we find it more reliable to concentrate on fitting of R_{xx}, since the data of ΔR_{xy} have a considerably greater measurement error compared to R_{xx}, because of relative smallness of ΔR_{xy}. The nonmonotonic experimental and theoretical plots in Fig. 12 indicate that even at $T = 28.7$ K the hydrodynamic transport regime is not yet reached. Indeed, the hydrodynamic theory describes a monotonic decrease of $-\Delta R_{xy}/R_{xy}^{(0)}$ with increasing magnetic field [14,28]; in particular, based on Eq. (19) one can find

$$\frac{\Delta R_{xy}}{R_{xy}^{(0)}} = -\frac{(2l/l_1)}{(\kappa L/2)/\tanh(\kappa L/2) + \kappa^2 L l_s/2 - 1}. \quad (21)$$

This dependence does not fit our experimental data at any slip length l_s, which is not surprising, since the hydrodynamic regime requires $l_1/l_e \gg 1$ and $l_e/L \ll 1$ while our calculations give $l_1/l_e \simeq 2$ and $l_e/L \simeq 1$ at $T = 28.7$ K (see Fig. 9). Nevertheless, the temperature-induced effects such as a rapid suppression of the peak of $-\Delta R_{xy}/R_{xy}^{(0)}$ and the change of sign of ΔR_{xy} at $B \to 0$ confirm that the influence of electron viscosity on transport properties is already significant.

IV. DISCUSSION AND CONCLUSIONS

Whereas the T^{-2} scaling of the effective electron-electron scattering time τ_e given by Eq. (20) follows from the general properties of Fermi liquids, the numerical coefficient A in this dependence is a subject of discussion. Our observation of the magnetoresistance behavior and its modification by temperature, together with a detailed comparison of experimental data with theory, suggest $A \simeq 5 - 6$, which, at first glance, seems to be an unexpectedly large value. Below we demonstrate why A actually can be large. For degenerate 2D electron gas, when $(T/\varepsilon_F)^2 \ll 1$, the dominant electron-electron scattering events are either "collinear" collisions, when the directions of motion of colliding particles are nearly equal and the scattering angle is small, or "head-to-head" collisions, when the directions of colliding particles are nearly opposite and the scattering angle is arbitrary. While the collinear collisions determine the quantum lifetime of electrons [36–38], they are not efficient in relaxation of the angular distribution of electrons, and the main contribution to the electron-electron collision integral comes from the head-to-head collisions [39,40]. The latter, however, can be significantly suppressed for the following reasons. First, the wave number transferred in the head-to-head collisions is of the order of Fermi wave number k_F, so when k_F exceeds either the inverse screening length $q_0 = 2/a_B$ (here a_B is the Bohr radius) or the inverse quantum well width $1/a$ [41], the scattering amplitude decreases. This is the case of our high-density samples, where $k_F \simeq 3/a$. Second, the effect of Cooper-channel renormalization of the scattering amplitude [42], applicable to head-to-head collisions, can enhance the effective electron-electron scattering time by a logarithmically large factor $\ln^2(\varepsilon_F/T)$ [43].

The suppression of electron-electron scattering described above makes it difficult to attain the fully hydrodynamic regime in GaAs samples, since an increase of temperature over 40–50 K turns on a strong scattering of electrons by optical phonons. Nevertheless, one may identify the intermediate regime, when $l_1 > l_e \sim L$ and the influence of electron-electron interaction on angular relaxation of electron distribution, promoting the effects of electronic viscosity, becomes considerable. In this regime, which is realized in our samples at $T = 20$–30 K, all the features characteristic for the quasiballistic (low-temperature) transport regime are suppressed with increasing temperature. The manifestations of the ballistic transport already described in the previous studies are: the peaks of both the longitudinal resistance R_{xx} and normalized Hall resistance $-\Delta R_{xy}/R_{xy}^{(0)}$, the sharp change of the slope of these peaks at $R_c = L/2$, the local minimum of R_{xx} at $B = 0$, and the negative sign of $-\Delta R_{xy}/R_{xy}^{(0)}$ at small B. To this list, we have added a previously unnoticed feature, the sharp change of the slope of the derivative dR_{xx}/dB at $R_c = L/4$. By combining theory and experiment, we have demonstrated that the kinetic equation approach, based on the relaxation-time approximation for the electron-electron collision integral, gives a reasonably accurate quantitative description of magnetoresistance as the latter evolves with temperature. A comparison of theory and experiment allows one to probe the contribution of electron-electron interaction into transport coefficients.

Whereas in the region of small magnetic fields the purely classical approach used above is valid, the increase of the magnetic field would lead to the quantum Hall regime [33]. A connection between classical magnetotransport in a channel with diffusive boundary reflection and quantum magnetotransport in a channel with the quantum Hall edge is not yet established theoretically, although some steps in this direction are already taken [44]. This challenging and important problem deserves proper attention in future studies.

ACKNOWLEDGMENTS

The authors acknowledge financial support of this work by FAPESP and CNPq (Brazilian agencies).

APPENDIX: EQUATIONS FOR POTENTIAL AND CURRENT DISTRIBUTION

This Appendix provides the details of derivation of Eqs. (15) and (16) and specifies the functions $\mathcal{K}_{nn'}(y, y')$ and $\mathcal{L}_n(y)$ standing in these equations. Also, the limiting transitions to the cases of zero magnetic field, semi-infinite plane, and wide channel are described.

The general solution of Eq. (11) is written as a sum of the general solution of homogeneous equation and a solution of inhomogeneous equation (for brevity, $R_c \equiv R$ below):

$$g_\varphi = \mathcal{D}(u)e^{-p\varphi} + \int_0^\varphi d\varphi' e^{p(\varphi'-\varphi)} R\mathcal{F}_{\varphi'}(y'),$$
$$p \equiv R/l, \quad u = y + R\cos\varphi, \quad y' = u - R\cos\varphi', \quad \text{(A1)}$$

where $\mathcal{D}(u)$ is an arbitrary function of its argument. To find this function, it is necessary to apply the boundary conditions. Before doing this, it is convenient to write the solution in the regions $0 < \varphi < \pi$ and $\pi < \varphi < 2\pi$ separately:

$$g_\varphi(y) = \mathcal{D}_0(y + R\cos\varphi)e^{-p\varphi} + \int_{\varphi_0}^{\varphi} d\varphi' \times e^{p(\varphi'-\varphi)} R\mathcal{F}_{\varphi'}(y'), \quad 0 < \varphi < \pi,$$
$$g_\varphi(y) = \mathcal{D}_1(y + R\cos\varphi)e^{-p\varphi} - \int_{\varphi}^{2\pi-\varphi_0} d\varphi' \times e^{p(\varphi'-\varphi)} R\mathcal{F}_{\varphi'}(y'), \quad \pi < \varphi < 2\pi. \quad \text{(A2)}$$

The requirement $y' \in [0, L]$ imposes restrictions on the range of φ'. Here we introduce important variables:

$$\varphi_0 = \arccos(\min\{1, \cos\varphi + y/R\}),$$
$$\varphi_L = \arccos(\max\{-1, \cos\varphi + (y - L)/R\}); \quad \text{(A3)}$$

both of them are functions of $y + R\cos\varphi$. If $0 < \varphi < \pi$, then $\varphi_0 = \varphi$ at the lower boundary, $y = 0$, and $\varphi_L = \varphi$ at the upper boundary, $y = L$. Inside the sample, $\varphi_0 < \varphi < \varphi_L$.

Application of the boundary conditions (12) and (13) defines $\mathcal{D}_0$ and $\mathcal{D}_1$. In the region $0 < \varphi < \pi$, the solution takes the form

$$g_\varphi(y) = \big(1-\mathrm{r}^0_{\varphi_0}\big)M_0 e^{p(\varphi_0-\varphi)}/\mathrm{d} + \big(1-\mathrm{r}^L_{\varphi_L}\big)M_L e^{p(2\varphi_0-\varphi-\varphi_L)}\mathrm{r}^0_{\varphi_0}/\mathrm{d} + \int_{\varphi_0}^{\varphi_L} d\varphi' R\mathcal{F}_{\varphi'}(y')\big\{[\theta(\varphi-\varphi')+(1-\mathrm{d})/\mathrm{d}]e^{p(\varphi'-\varphi)} + \mathrm{r}^0_{\varphi_0}e^{p(2\varphi_0-\varphi-\varphi')}/\mathrm{d}\big\}, \tag{A4}$$

$$g_{2\pi-\varphi}(y) = \big(1-\mathrm{r}^L_{\varphi_L}\big)M_L e^{p(\varphi-\varphi_L)}/\mathrm{d} + \big(1-\mathrm{r}^0_{\varphi_0}\big)M_0 e^{p(\varphi+\varphi_0-2\varphi_L)}\mathrm{r}^L_{\varphi_L}/\mathrm{d} + \int_{\varphi_0}^{\varphi_L} d\varphi' R\mathcal{F}_{\varphi'}(y')\big\{[\theta(\varphi'-\varphi)+(1-\mathrm{d})/\mathrm{d}]e^{p(\varphi-\varphi')} + \mathrm{r}^L_{\varphi_L}e^{p(\varphi+\varphi'-2\varphi_L)}/\mathrm{d}\big\}. \tag{A5}$$

Transforming the integrals over φ' into the integrals over y', one also obtains

$$g_\varphi(y) = \big(1-\mathrm{r}^0_{\varphi_0}\big)M_0 e^{p(\varphi_0-\varphi)}/\mathrm{d} + \big(1-\mathrm{r}^L_{\varphi_L}\big)M_L e^{p(2\varphi_0-\varphi-\varphi_L)}\mathrm{r}^0_{\varphi_0}/\mathrm{d} + \int_0^L dy' Q^0_\varphi(y,y')\mathcal{F}_{\varphi'}(y'), \tag{A6}$$

$$g_{2\pi-\varphi}(y) = \big(1-\mathrm{r}^L_{\varphi_L}\big)M_L e^{p(\varphi-\varphi_L)}/\mathrm{d} + \big(1-\mathrm{r}^0_{\varphi_0}\big)M_0 e^{p(\varphi+\varphi_0-2\varphi_L)}\mathrm{r}^L_{\varphi_L}/\mathrm{d} + \int_0^L dy' Q^1_\varphi(y,y')\mathcal{F}_{\varphi'}(y'). \tag{A7}$$

In these expressions,

$$\mathrm{d} = 1 - \mathrm{r}^0_{\varphi_0}\mathrm{r}^L_{\varphi_L}e^{2p(\varphi_0-\varphi_L)}, \tag{A8}$$

and

$$Q^0_\varphi(y,y') = \big\{[\theta(\varphi-\varphi')+(1-\mathrm{d})/\mathrm{d}]e^{p(\varphi'-\varphi)} + \mathrm{r}^0_{\varphi_0}e^{p(2\varphi_0-\varphi-\varphi')}/\mathrm{d}\big\}\frac{1}{\sin\varphi'}, \tag{A9}$$

$$Q^1_\varphi(y,y') = \big\{[\theta(\varphi'-\varphi)+(1-\mathrm{d})/\mathrm{d}]e^{p(\varphi-\varphi')} + \mathrm{r}^L_{\varphi_L}e^{p(\varphi+\varphi'-2\varphi_L)}/\mathrm{d}\big\}\frac{1}{\sin\varphi'}, \tag{A10}$$

with

$$\varphi' = \arccos[\cos\varphi + (y-y')/R]. \tag{A11}$$

It is implied that the kernels Q^0 and Q^1 are equal to zero outside the region $u - R < y' < u + R$, since only in this region the definition of φ' makes sense. Since $y - R < u < y + R$, this also means that Q^0 and Q^1 are nonzero within the interval $|y' - y| < 2R$, so that the actual upper and lower limits of the integration over y' are $y'_{\max} = \min\{L, y + 2R\}$ and $y'_{\min} = \max\{0, y - 2R\}$, respectively. The correlation length of $2R$ is characteristic for the case $R < l$. However, if $R > l$, the correlation length is of the order of the mean free path length l, because Q^0 and Q^1 exponentially decrease with $|y' - y|/l$.

At the boundaries,

$$g_{2\pi-\varphi}(0) = \frac{1}{\mathrm{d}_0}\big[\big(1-\mathrm{r}^L_{\varphi_{L0}}\big)M_L e^{p(\varphi-\varphi_{L0})} + \big(1-\mathrm{r}^0_\varphi\big)M_0(1-\mathrm{d}_0)/\mathrm{r}^0_\varphi\big] + \int_0^L dy' \frac{\mathcal{F}_{\varphi'_0}(y')}{\mathrm{d}_0\sin\varphi'_0}\left[e^{p(\varphi-\varphi'_0)} + e^{p(\varphi'_0-\varphi)}\frac{1-\mathrm{d}_0}{\mathrm{r}^0_\varphi}\right], \tag{A12}$$

$$g_\varphi(L) = \frac{1}{\mathrm{d}_L}\big[\big(1-\mathrm{r}^0_{\varphi_{0L}}\big)M_0 e^{p(\varphi_{0L}-\varphi)} + \big(1-\mathrm{r}^L_\varphi\big)M_L(1-\mathrm{d}_L)/\mathrm{r}^L_\varphi\big] + \int_0^L dy' \frac{\mathcal{F}_{\varphi'_L}(y')}{\mathrm{d}_L\sin\varphi'_L}\left[e^{p(\varphi'_L-\varphi)} + e^{p(\varphi-\varphi'_L)}\frac{1-\mathrm{d}_L}{\mathrm{r}^L_\varphi}\right], \tag{A13}$$

where φ_{L0}, φ'_0, and d_0 denote φ_L, φ', and d at $y = 0$, respectively, while φ_{0L}, φ'_L, and d_L denote φ_0, φ', and d at $y = L$. The expressions (A12) and (A13) can be used to find the constants M_0 and M_L according to Eq. (14). This leads to the following linear equations:

$$\begin{aligned}(\mathcal{N}_0-\alpha_0)M_0 - \beta_0 M_L &= \kappa_0,\\ -\beta_L M_0 + (\mathcal{N}_L-\alpha_L)M_L &= \kappa_L,\end{aligned} \tag{A14}$$

where

$$\alpha_0 = \int_0^\pi \frac{d\varphi}{\mathrm{d}_0}\big(1-\mathrm{r}^0_\varphi\big)^2\mathrm{r}^L_{\varphi_{L0}}\sin\varphi e^{2p(\varphi-\varphi_{L0})},$$

$$\alpha_L = \int_0^\pi \frac{d\varphi}{\mathrm{d}_L}\big(1-\mathrm{r}^L_\varphi\big)^2\mathrm{r}^0_{\varphi_{0L}}\sin\varphi e^{2p(\varphi_{0L}-\varphi)},$$

$$\beta_0 = \int_0^\pi \frac{d\varphi}{\mathrm{d}_0}\big(1-\mathrm{r}^0_\varphi\big)\big(1-\mathrm{r}^L_{\varphi_{L0}}\big)\sin\varphi e^{p(\varphi-\varphi_{L0})},$$

$$\beta_L = \int_0^\pi \frac{d\varphi}{\mathrm{d}_L}\big(1-\mathrm{r}^L_\varphi\big)\big(1-\mathrm{r}^0_{\varphi_{0L}}\big)\sin\varphi e^{p(\varphi_{0L}-\varphi)}, \tag{A15}$$

and

$$\kappa_0 = \int_0^\pi d\varphi\big(1-\mathrm{r}^0_\varphi\big)\sin\varphi\int_0^L dy'\frac{\mathcal{F}_{\varphi'_0}(y')}{\mathrm{d}_0\sin\varphi'_0} \times\big[e^{p(\varphi-\varphi'_0)} + e^{p(\varphi'_0-\varphi)}(1-\mathrm{d}_0)/\mathrm{r}^0_\varphi\big],$$

$$\kappa_L = \int_0^\pi d\varphi\big(1-\mathrm{r}^L_\varphi\big)\sin\varphi\int_0^L dy'\frac{\mathcal{F}_{\varphi'_L}(y')}{\mathrm{d}_L\sin\varphi'_L} \times\big[e^{p(\varphi'_L-\varphi)} + e^{p(\varphi-\varphi'_L)}(1-\mathrm{d}_L)/\mathrm{r}^L_\varphi\big]. \tag{A16}$$

If two boundaries are equivalent, the following relations are valid:

$$\alpha_L = \alpha_0, \quad \beta_L = \beta_0, \quad \kappa_L = -\kappa_0. \tag{A17}$$

To prove the first two equalities, it is sufficient to substitute $\varphi \to \pi - \varphi$ under the integrals in Eq. (A15). This transformation does not affect r_φ and $\sin\varphi$, while leading to $\cos\varphi \to -\cos\varphi$ and $\varphi_{L0} \to \pi - \varphi_{0L}$ so that $\cos\varphi_{L0} \to -\cos\varphi_{0L}$. To prove that $\kappa_L = -\kappa_0$, one should also substitute $y' \to L - y'$ under the integrals over y' in Eq. (A16), which leads to $\varphi_0' \to \pi - \varphi_L'$, and to notice that $\mathcal{F}_\varphi(y) = -\mathcal{F}_{\pi-\varphi}(L-y)$. With $\mathcal{N}_0 = \mathcal{N}_L \equiv \mathcal{N}$, $\alpha_0 = \alpha_L \equiv \alpha$, $\beta_0 = \beta_L \equiv \beta$, $\eta_0 \equiv \eta$, and $\kappa_0 \equiv \kappa$, one obtains

$$M_0 = -M_L = \frac{\eta + \kappa}{\mathcal{N} - \alpha + \beta}. \tag{A18}$$

In the general case, one may introduce numerical coefficients $Z = (\mathcal{N}_0 - \alpha_0)(\mathcal{N}_L - \alpha_L) - \beta_0\beta_L$, $a_{00} = (\mathcal{N}_L - \alpha_L)/Z$, $a_{L0} = \beta_L/Z$, $a_{0L} = \beta_0/Z$, and $a_{LL} = (\mathcal{N}_0 - \alpha_0)/Z$, and then

$$M_0 = a_{00}\kappa_0 + a_{0L}\kappa_L, \; M_L = a_{L0}\kappa_0 + a_{LL}\kappa_L. \tag{A19}$$

The solutions presented above lead to the integral equations (15) and (16) with ($n = 0, 1$, $n' = 0, 1$)

$$\begin{aligned}\mathcal{K}_{nn'}(y,y') = {} & \int_0^\pi \frac{d\varphi}{2\pi}(2\cos\varphi)^n(\cos\varphi')^{n'}Q_\varphi^+(y,y') \\ & + \left[\mu_0^n(y)a_{00} + \mu_L^n(y)a_{L0}\right]\zeta_0^{n'}(y') \\ & + \left[\mu_0^n(y)a_{0L} + \mu_L^n(y)a_{LL}\right]\zeta_L^{n'}(y'),\end{aligned} \tag{A20}$$

$$\begin{aligned}\mathcal{L}_n(y) = {} & \int_0^\pi \frac{d\varphi}{2\pi}\int_0^L dy'(2\cos\varphi)^n\cos\varphi' Q_\varphi^+(y,y') \\ & + \left[\mu_0^n(y)a_{00} + \mu_L^n(y)a_{L0}\right]\int_0^L dy'\zeta_0^1(y') \\ & + \left[\mu_0^n(y)a_{0L} + \mu_L^n(y)a_{LL}\right]\int_0^L dy'\zeta_L^1(y'),\end{aligned} \tag{A21}$$

where $Q_\varphi^+(y,y') = Q_\varphi^0(y,y') + Q_\varphi^1(y,y')$,

$$\begin{aligned}\mu_0^n(y) = {} & \int_0^\pi d\varphi(2\cos\varphi)^n\frac{1-\mathrm{r}_{\varphi_0}^0}{2\pi\,\mathrm{d}} \\ & \times\left[e^{p(\varphi_0-\varphi)} + \mathrm{r}_{\varphi_L}^L e^{p(\varphi+\varphi_0-2\varphi_L)}\right],\end{aligned} \tag{A22}$$

$$\begin{aligned}\mu_L^n(y) = {} & \int_0^\pi d\varphi(2\cos\varphi)^n\frac{1-\mathrm{r}_{\varphi_L}^L}{2\pi\,\mathrm{d}} \\ & \times\left[\mathrm{r}_{\varphi_0}^0 e^{p(2\varphi_0-\varphi-\varphi_L)} + e^{p(\varphi-\varphi_L)}\right],\end{aligned} \tag{A23}$$

$$\begin{aligned}\zeta_0^n(y') = {} & \int_0^\pi d\varphi\left(1-\mathrm{r}_\varphi^0\right)\frac{\sin\varphi(\cos\varphi_0')^n}{\mathrm{d}_0\sin\varphi_0'} \\ & \times\left[e^{p(\varphi-\varphi_0')} + e^{p(\varphi_0'-\varphi)}(1-\mathrm{d}_0)/\mathrm{r}_\varphi^0\right],\end{aligned} \tag{A24}$$

$$\begin{aligned}\zeta_L^n(y') = {} & \int_0^\pi d\varphi\left(1-\mathrm{r}_\varphi^L\right)\frac{\sin\varphi(\cos\varphi_L')^n}{\mathrm{d}_L\sin\varphi_L'} \\ & \times\left[e^{p(\varphi_L'-\varphi)} + e^{p(\varphi-\varphi_L')}(1-\mathrm{d}_L)/\mathrm{r}_\varphi^L\right],\end{aligned} \tag{A25}$$

The functions ζ_0^n and ζ_L^n depend on y' through φ_0' and φ_L'.

A transition to the limit $B = 0$, when $R \to \infty$, is carried out by using the approximate expressions

$$\begin{aligned}\varphi - \varphi' = (y - y')/R\sin\varphi, \quad \varphi_0 = \varphi - y/R\sin\varphi, \\ \varphi_L = \varphi - (y-L)/R\sin\varphi,\end{aligned} \tag{A26}$$

valid at $R \gg |y - y'|$ (which always takes place at $R \gg L$) provided that $\sin\varphi$ is not very small. In this limit, the difference between φ_0, φ_L, φ, and φ' goes to zero, but this difference still has to be taken into account in the exponential factors in order to compensate the large parameter $p = R/l$. Thus, in the lowest order in L/R, the quantity R drops out from the equations and the general solution is written in the form

$$g_\varphi(y) = g_\varphi(0)e^{-y/l\sin\varphi} + \frac{1}{\sin\varphi}\int_0^y dy' e^{(y'-y)/l\sin\varphi}\mathcal{F}_\varphi(y'), \tag{A27}$$

$$\begin{aligned}g_{2\pi-\varphi}(y) = {} & g_{2\pi-\varphi}(L)e^{(y-L)/l\sin\varphi} \\ & + \frac{1}{\sin\varphi}\int_y^L dy' e^{(y-y')/l\sin\varphi}\mathcal{F}_\varphi(y'),\end{aligned} \tag{A28}$$

with $\varphi \in [0, \pi]$. The boundary conditions are simplified at $B = 0$, since the integral terms M_0 and M_L disappear. From these conditions, we determine the constants $g_\varphi(0)$ and $g_{2\pi-\varphi}(L)$ and obtain

$$\begin{aligned}g_\varphi(y) = {} & \int_0^L dy' Q_\varphi^0(y,y')\mathcal{F}_\varphi(y'), \\ g_{2\pi-\varphi}(y) = {} & \int_0^L dy' Q_\varphi^1(y,y')\mathcal{F}_\varphi(y'),\end{aligned} \tag{A29}$$

where

$$\begin{aligned}Q_\varphi^0(y,y') = {} & \left\{[\theta(y-y') + (1-\mathrm{d})/\mathrm{d}]e^{(y'-y)/l\sin\varphi}\right. \\ & \left. + \mathrm{r}_\varphi^0 e^{-(y+y')/l\sin\varphi}/\mathrm{d}\right\}\frac{1}{\sin\varphi},\end{aligned} \tag{A30}$$

$$\begin{aligned}Q_\varphi^1(y,y') = {} & \left\{[\theta(y'-y) + (1-\mathrm{d})/\mathrm{d}]e^{(y-y')/l\sin\varphi}\right. \\ & \left. + \mathrm{r}_\varphi^L e^{(y+y'-2L)/l\sin\varphi}/\mathrm{d}\right\}\frac{1}{\sin\varphi},\end{aligned} \tag{A31}$$

with

$$\mathrm{d} = 1 - \mathrm{r}_\varphi^0\mathrm{r}_\varphi^L\lambda_\varphi^2, \quad \lambda_\varphi = e^{-L/l\sin\varphi}. \tag{A32}$$

The integral equation (15) is reduced to

$$g_0(y) = \frac{1}{l}\int_0^L dy'\mathcal{K}_{00}(y,y')g_0(y'),$$

which has a trivial solution $g_0(y) = 0$. Strictly speaking, an arbitrary constant also satisfies this equation, but this is not essential because $g_0(y)$ is defined with the accuracy up to a constant. The integral equation (16) is reduced to Eq. (17) for $g_1(y)$. There,

$$\begin{aligned}\mathcal{K}_{11}(y,y') = {} & \int_0^\pi \frac{d\varphi}{\pi}\frac{\cos^2\varphi}{\sin\varphi}\left[e^{-|y-y'|/l\sin\varphi}\right. \\ & + 2\cosh(|y-y'|/l\sin\varphi)(1-\mathrm{d})/\mathrm{d} \\ & \left. + \mathrm{r}_\varphi^0 e^{-(y+y')/l\sin\varphi}/\mathrm{d} + \mathrm{r}_\varphi^L e^{(y+y'-2L)/l\sin\varphi}/\mathrm{d}\right]\end{aligned} \tag{A33}$$

and

$$\mathcal{L}_1(y) = l\int_0^\pi \frac{d\varphi}{\pi}\cos^2\varphi\left[2-\xi_\varphi^L e^{(y-L)/l\sin\varphi}-\xi_\varphi^0 e^{-y/l\sin\varphi}\right],$$
$$\xi_\varphi^{0,L} = \left[1-\mathrm{r}_\varphi^{0,L}(1-\lambda_\varphi)-\mathrm{r}_\varphi^0\mathrm{r}_\varphi^L\lambda_\varphi\right]/\mathrm{d}, \tag{A34}$$

in accordance with [2].

The formalism given above also allows for treatment of a semi-infinite plane, when a single boundary at $y=0$ is present. In this case, one should formally put $\varphi_L=\pi, \mathrm{r}_{\varphi_L}^L=1$, and extend the upper limit of the integration over y' to infinity. The factor M_L does not enter the distribution function because it always stands at $1-\mathrm{r}_{\varphi_L}^L$, while M_0, in view of $\beta_0=\beta_L=0$, is given by $M_0=a_{00}\kappa_0$, $a_{00}=1/(\mathcal{N}_0-\alpha_0)$. Notice that in this case

$$\mathcal{N}_0-\alpha_0 = \int_0^\pi d\varphi\left(1-\mathrm{r}_\varphi^0\right)\sin\varphi(1-e^{2p(\varphi-\pi)})/\mathrm{d}_0,$$
$$\mathrm{d}_0 = 1-\mathrm{r}_\varphi^0 e^{2p(\varphi-\pi)}. \tag{A35}$$

In Eqs. (A20) and (A21), only the parts containing $Q_\varphi^+(y,y')$ and a_{00} survive.

Far from the boundaries, the electrons are moving in the cyclotron orbits and do not feel the boundaries. Formally, this case is described by the substitutions $\varphi_0=0, \varphi_L=\pi, \mathrm{r}_{\varphi_0}^0=1$, and $\mathrm{r}_{\varphi_L}^L=1$ so that

$$\mathcal{K}_{00}(y,y') = \int_0^\pi \frac{d\varphi}{2\pi}\frac{\Lambda_{\varphi\varphi'}}{\sin\varphi'},$$
$$\Lambda_{\varphi\varphi'} = \frac{1}{\mathrm{d}}[e^{-p|\varphi'-\varphi|}+e^{p(|\varphi'-\varphi|-2\pi)}$$
$$+e^{-p(\varphi'+\varphi)}+e^{p(\varphi'+\varphi-2\pi)}], \tag{A36}$$

where $\mathrm{d}=1-e^{-2\pi p}$ is constant. The other kernels, $\mathcal{K}_{10}(y,y')$, $\mathcal{K}_{01}(y,y')$, and $\mathcal{K}_{11}(y,y')$ are given by the same expression with extra multipliers $2\cos\varphi$, $\cos\varphi'$, and $2\cos\varphi\cos\varphi'$ under the integral, respectively. As already mentioned, $\mathcal{K}_{nn'}(y,y')$ are nonzero only at $|y'-y|<2R$. Using the identity

$$\int_0^\pi d\varphi\Lambda_{\varphi\varphi'} = \int_0^\pi d\varphi'\Lambda_{\varphi\varphi'} = \frac{2}{p}, \tag{A37}$$

one can show that Eqs. (15) and (16) are satisfied for linear Hall voltage, $g_0(y)=C+eEyl_1/R$, and constant current, $g_1(y)=eEl_1$. This means that in the bulk of the sample the current and the Hall field are the same as in an infinitely wide sample, while within the layers of widths $4R$ near the boundaries the current and the Hall field are coordinate dependent.

[1] R. N. Gurzhi, Sov. Phys. JETP **44**, 771 (1963); Sov. Phys. Usp. **11**, 255 (1968).
[2] M. J. M. de Jong and L. W. Molenkamp, Phys. Rev. B **51**, 13389 (1995).
[3] A. O. Govorov and J. J. Heremans, Phys. Rev. Lett. **92**, 026803 (2004).
[4] M. Müller, J. Schmalian, and Lars Fritz, Phys. Rev. Lett. **103**, 025301 (2009).
[5] R. Bistritzer and A. H. MacDonald, Phys. Rev. B **80**, 085109 (2009).
[6] A. V. Andreev, S. A. Kivelson, and B. Spivak, Phys. Rev. Lett. **106**, 256804 (2011).
[7] B. N. Narozhny, I. V. Gornyi, M. Titov, M. Schütt, and A. D. Mirlin, Phys. Rev. B **91**, 035414 (2015).
[8] I. Torre, A. Tomadin, A. K. Geim, and M. Polini, Phys. Rev. B **92**, 165433 (2015).
[9] D. A. Bandurin, I. Torre, R. Krishna Kumar, M. Ben Shalom, A. Tomadin, A. Principi, G. H. Auton, E. Khestanova, K. S. Novoselov, I. V. Grigorieva, L. A. Ponomarenko, A. K. Geim, and M. Polini, Science **351**, 1055 (2016).
[10] P. S. Alekseev, Phys. Rev. Lett. **117**, 166601 (2016).
[11] A. Lucas, J. Crossno, K. C. Fong, P. Kim, and S. Sachdev, Phys. Rev. B **93**, 075426 (2016).
[12] A. Principi, G. Vignale, M. Carrega, and M. Polini, Phys. Rev. B **93**, 125410 (2016).
[13] F. M. D. Pellegrino, I. Torre, A. K. Geim, and M. Polini, Phys. Rev. B **94**, 155414 (2016).
[14] T. Scaffidi, N. Nandi, B. Schmidt, A. P. Mackenzie, and J. E. Moore, Phys. Rev. Lett. **118**, 226601 (2017).
[15] G. Falkovich and L. Levitov, Phys. Rev. Lett. **119**, 066601 (2017).
[16] A. Levchenko, H.-Y. Xie, and A. V. Andreev, Phys. Rev. B **95**, 121301(R) (2017).
[17] A. Lucas, Phys. Rev. B **95**, 115425 (2017).
[18] D. A. Bandurin, A. V. Shytov, L. S. Levitov, R. Krishna Kumar, A. I. Berdyugin, M. Ben Shalom, I. V. Grigorieva, A. K. Geim, and G. Falkovich, Nature Comm. **9**, 4533 (2018).
[19] A. Lucas and S. A. Hartnoll, Phys. Rev. B **97**, 045105 (2018).
[20] A. Lucas and K. C. Fong, J. Phys.: Condens. Matter **30**, 053001 (2018).
[21] G. M. Gusev, A. D. Levin, E. V. Levinson, and A. K. Bakarov, AIP Adv. **8**, 025318 (2018).
[22] G. M. Gusev, A. D. Levin, E. V. Levinson, and A. K. Bakarov, Phys. Rev. B **98**, 161303(R) (2018).
[23] A. D. Levin, G. M. Gusev, E. V. Levinson, Z. D. Kvon, and A. K. Bakarov, Phys. Rev. B **97**, 245308 (2018).
[24] P. S. Alekseev and M. A. Semina, Phys. Rev. B **98**, 165412 (2018).
[25] P. S. Alekseev and M. A. Semina, Phys. Rev. B **100**, 125419 (2019).
[26] M. Chandra, G. Kataria, D. Sahdev, and R. Sundararaman, Phys. Rev. B **99**, 165409 (2019).
[27] I. S. Burmistrov, M. Goldstein, M. Kot, V. D. Kurilovich, and P. D. Kurilovich, Phys. Rev. Lett. **123**, 026804 (2019).
[28] T. Holder, R. Queiroz, T. Scaffidi, N. Silberstein, A. Rozen, J. A. Sulpizio, L. Ella, S. Ilani, and A. Stern, Phys. Rev. B **100**, 245305 (2019).
[29] S. B. Soffer, J. Appl. Phys. **38**, 1710 (1967).
[30] L. A. Fal'kovskii, Sov. Phys. JETP **31**, 981 (1970).
[31] V. I. Okulov and V. V. Ustinov, Sov. Phys. JETP **40**, 584 (1975).
[32] K. Fuchs, Proc. Cambridge Phil. Soc. **34**, 100 (1938).
[33] C. W. J. Beenakker and H. van Houten, Solid State Physics **44**, 1 (1991).

[34] E. Ditlefsen and J. Lothe, Phil. Mag. **14**, 759 (1966).
[35] T. J. Thornton, M. L. Roukes, A. Scherer, and B. P. Van de Gaag, Phys. Rev. Lett. **63**, 2128 (1989).
[36] G. F. Giuliani and J. J. Quinn, Phys. Rev. B **26**, 4421 (1982).
[37] L. Zheng and S. Das Sarma, Phys. Rev. B **53**, 9964 (1996).
[38] T. Jungwirth and A. H. MacDonald, Phys. Rev. B **53**, 7403 (1996).
[39] R. N. Gurzhi, A. N. Kalinenko, and A. I. Kopeliovich, Phys. Rev. Lett. **74**, 3872 (1995).
[40] R. N. Gurzhi, A. N. Kalinenko, and A. I. Kopeliovich, Low Temp. Phys. **23**, 44 (1997).
[41] A suppression of the matrix element of electron-electron scattering with increasing quantum well width is described, for example, by S. M. Goodnick and P. Lugli, Phys. Rev. B **37**, 2578 (1988).
[42] I. L. Aleiner and K. B. Efetov, Phys. Rev. B **74**, 075102 (2006).
[43] D. S. Novikov, Viscosity of a two-dimensional Fermi liquid, arXiv:cond-mat/0603184.
[44] T. Stegmann, D. E. Wolf, and A. Lorke, New J. Phys. **15**, 113047 (2013).